435

Acta Chim. Slov. **1999**, *46*(3), pp. 435-461

HIGH-RESOLUTION TRANSMISSION ELECTRON MICROSCOPY (HRTEM): IMAGE PROCESSING ANALYSIS OF DEFECTS AND GRAIN BOUNDARIES IN NANOCRYSTALLINE MATERIALS*

Anđelka Tonejc

Faculty of Science, Department of Physics, Bijenička c. 32, 10000 Zagreb, Croatia

(Received 10.5.1999)

Abstract. A brief overview of the application of the high resolution transmission electron microscopy (HRTEM) method is given: the principle of HRTEM image formation in an electron microscope; different modes of image formation; the role of contrast transfer function (CTF) in HRTEM image formation; definition and improvement of electron microscope resolution. As an example, the image processing of HRTEM micrographs of mechanically alloyed ZrO_2-10mol% Y_2O_3 powders was performed in order to obtain information about alloying and transformation at the atomic level.

In this work the results obtained by applying the CRISP program to analyse the HRTEM photographs of mechanically alloyed nanocrystalline materials are presented. The investigation is focused on the following regions: a) the grain boundary region; b) the region of stacking faults; c) the region of overlapping layers of zirconia and yttria.

Fourier filtering revealed at the atomic level one possible sequence of alloying that occurred at the grain boundary, on the stacking faults and in the overlapping layers. Performing the Fourier filtering with different filtering mask, it was possible to isolate the separate planes introduced into the correct order of particular family of m-ZrO_2 lattice. The introduced planes belonging to m-ZrO_2 or Y_2O_3 could be regarded as dislocations introduced into the perfect m-ZrO_2 lattice. Since they were identified in corresponding FT, from which the filtering was performed, it was possible to give an interpretation about the transformation due to the mechanical alloying observed in the particular HRTEM image.

1. Introduction

In the last ten years the construction of electron microscopes (EM) was highly improved and the resolution reached 0.11 nm. The modern electron microscopes are

*Plenary lecture held at the 7th Slovenian-Croatian Crystallographic Meeting, Radenci, Slovenia, June 18-20, 1998.

constructed to work with acceleration voltages as high as 200 kV, 300 kV, 400kV and even 1250 kV ("atomic resolution" microscope).

A transmission electron microscope uses a series of electromagnetic lenses to manipulate the electron beam generated at a high potential in an electrically heated filament. Depending on imaging conditions either the particle or wave properties of the emitted electrons have to be considered. The wavelength of the electrons depends on the acceleration voltage ($\lambda=h/(2meV)^{1/2}$). As an electron wave penetrates the sample, the resulting diffraction pattern reveals the structure of the observed sample.

Analysing the image and the corresponding diffraction one can obtain useful information on the grain sizes, the precipitates, the orientation of precipitates to the matrix and on the appearance of superstructure. With the aid of the energy dispersive X-ray attachment (analytical microscope) it is also possible to measure qualitatively and quantitatively the concentration and composition of elements, using the characteristic X-ray spectra.

In the transmission electron microscope, one can simultaneously obtain the image and the corresponding diffraction pattern from the same part of the sample, and the concentration of elements in the sample, as well as the mapping of the elements in the same region of the sample. The mapping of the elements is also possible with the scanning probe resolution of 1 nm. Related to the particular diffraction pattern it is possible to obtain the bright field (BF) and dark field (DF) image. Under special imaging conditions (large incident convergent beam, a thicker region of the sample) it is also possible to obtain the convergent beam electron diffraction pattern (CBED).

HRTEM provides a direct evidence in the local structure and its irregularities at the atomic scale. HRTEM images taken under optimal weak-phase-object conditions, at Scherzer defocus, represent the projected potential of the crystal and can be used for structure determination of an unknown crystal.

HRTEM observations are of special interest in solid state physics, solid state chemistry and materials science because of the importance of the investigation of the relationships between the microstructure and the properties of the solids, particularly in the influence of the different kinds of structural defects on macroscopic behaviour.

The following [1] illustrates the wide-spread applicability of HRTEM in crystallography as well as in materials science, including solid state physics and chemistry, mineralogy, and life science: structure analysis (refinement) of crystalline and amorphous materials; characterisation of the real structure, especially of structure defects; analysis of internal interface structure (homo- and hetero-phase boundaries); investigation of the dislocation core structure; phase analysis (information on local chemical composition); detection of superstructures; investigation of phase transitions (crystalline-crystalline, crystalline-amorphous, including polymorphism); detection of order-disorder phenomena; structure investigation of non stoichiometric compounds; investigation of dynamic processes (e.g. in situ observation of crystal growth); imaging of single atoms and atom clusters; detection of point defects and point defect agglomerates.

For crystallography, it is important that high resolution electron microscopy (HRTEM) and electron diffraction (ED) with crystallographic image processing (CIP), could solve, under some condition, an unknown crystal structure.

The first structure was solved by ED in 1949 by Vainstein and Pinsker [2]. Since then a lot of results were obtained in this field [3,4] and different methods were applied. It has been shown that HRTEM combined with crystallographic image processing (CIP) can be used to determine co-ordinates of metal atoms in oxides with an accuracy of about 0.01 nm [5].

In 1992 Wenk [6,7] et al. were the first to combine 2D HRTEM images into 3D reconstruction for solving the structure of an inorganic crystal, mineral staurolite. In the 3D map all atoms (Fe, Al, Si, oxygen) were clearly resolved (at the resolution of 0.138 nm).

With the development of electron microscopes it is now possible to determine an unknown crystal structure with the accuracy of 0.002 nm [8]. In the last years, more and more structures were solved from HRTEM images and ED.

Convergent beam electron diffraction (CBED) has also been developed for structure analysis. CBED can provide information on the lattice parameters and crystal symmetry. It is more favourable to the thick crystal (larger than 50 nm) with a small unit

cell (smaller than 1 nm). Structure analysis by CBED has been summarised in two review articles [9,10].

The other problems are related to the resolution of an electron microscope as an instrument. The resolution depends mainly on the accelerating voltage and the aberration of objective lens (especially spherical aberration coefficient C_s and chromatic aberration coefficient C_c). Questions related to the utilisation of HRTEM and ED, as was listed before, are related to the resolution of the instrument, when the crystal structure is known.

What can be really resolved in the HRTEM image? Now, for the medium voltage microscope of 200 kV the resolution is below 0.2 nm, and in the atomic resolution microscope, as the one installed in Stuttgart, working at 1250 kV [11,12], one approaches the atomic resolution of 0.1 nm.

The electron crystallography has two important advantages over X-ray crystallography for the determination of atomic positions in crystal structure: crystallographic phases can be determined directly from HRTEM images and the samples having dimensions 0.1x0.1x0.1 μm^3 can be analysed [3]. Contrary to that, for single crystal X- ray diffraction the crystal should have sizes larger than 100x100x100 μm^3.

The present paper deals with HRTEM and selected area electron diffraction applied in kinematics conditions and under weak phase object approximation of a thin object. The CRISP programme [13] used in the image processing analysis works under these conditions. An application of HRTEM image processing analyses for extracting some information on mechanically alloyed materials is given in the third part of this paper.

2. General Consideration About EM and HRTEM

2.1. Image Contrasts in EM

There are two important mechanisms which produce image contrast in the electron microscope:

i) *Diffraction contrast:* Diffracted electrons leaving at the lower surface of the crystalline specimen are intercepted by the objective aperture and prevented to contribute to the image. Only few of the diffracted beams form the image. The image contrast is produced by changes in absorption coefficient from one to another region of the specimen. At medium and low resolution the contrast in the image would arise from amplitude reduction in region of large scattering where the scattered rays are intercepted by the objective aperture.

ii) *Phase contrast:* Some of the diffracted beams leaving the specimen are recombined to form the image so that the phase difference present at the exit surface of the specimen is converted into intensity difference in the image. Phase contrast arises from the interference between waves included within the objective aperture and whose plane should be controlled by an accurate focusing to produce a contrast.

Diffraction contrast is the dominant mechanism revealing object details larger than 1.5 nm in crystalline specimens. It was widely used for study of crystal defects [14]. Phase contrast is the dominant mechanism for an object detail smaller than 1 nm and is important in high-resolution studies, in early stages of short-range order and amorphous materials. Phase contrast is the basic mechanism describing image formation in high resolution electron microscopy [1,15-20].

The solution of Schrödinger equation in the vacuum for electrons in an EM is :

$$\psi_0(r) = \exp(i\, \mathbf{k_0}\, \mathbf{r})$$

General solution of Schrödinger equation in Born approximation (electrons energy $E \gg e\,\varphi(r)$) of periodic potential $\varphi(\mathbf{r})$ is :

$$\psi(r) = \sum_{l} A_l \exp\left[i\phi_l + i\,(\mathbf{k_0} + \mathbf{g}_l)\,\mathbf{r}\right]$$

A_l are the amplitudes, ϕ_l are the phases of transmitted and the diffracted electron beams, g_l is the reciprocal vector of the l-th beam, where $l \neq 0$ is the order of the diffracted beam, and $l=0$ is transmitted beam. The wave function at the exit face of the sample, in this approach [17], is considered as a synthesis of different l-components of diffracted waves. Now we can go to image formation in the EM.

Amplitude (diffraction) contrast results from a filtering process whereby some of the electrons from the incoming electron beams are unable to reach the image plane. In normal (low resolution) bright field electron microscopy only the direct electron beam is allowed (l=0) to reach the image plane; all the scattered electrons are excluded by the objective lens aperture. In normal dark-field microscopy, the direct electron beam is excluded from the image plane and only one or more scattered beams having determined $\mathbf{g}_l$ are allowed to pass through the objective- lens aperture. The selection of scattered beams is performed by tilting the direct beam, or by moving the aperture so that the direct beam is blocked.

For high resolution imaging it is desirable to obtain as much structural information as possible about the specimen. This means allowing the maximum number of diffracted beams $\mathbf{g}_l$ to pass through the objective-lens aperture to form an image in the image plane (see Fig. 1 (b, c, d and e)). Further explanation will be given in HRTEM image formation 2.3.

2.2. Phase Object Approximation

Some approximation simplify the mathematical description of the scattering of the electrons by crystals. Here we assume that the crystals are pure phase objects [17-20], i.e. electrons passing through the crystal suffer only a phase shift; this is the phase object approximation (POA). The POA demands that electrons are only elastically scattered and the energy of electrons is so high that scattered electron waves are almost parallel to the incident wave.

If the electron beam has the direction of z-axes, the phase $\Delta\Phi(x,y)$ at the exit of the sample, having thickness $t = cN_z$, (N_z is number of unit cells in direction of z), is expressed as follows:

$$\Delta\Phi(x,y) = 2\ me\ \lambda\ h^{-2}\ N_z\ \varphi(x,y) = \sigma\ N_z\ \varphi(x,y)$$

The interaction constant $\sigma = 2\pi\ me\lambda / h^2$, where m, e, λ, are the mass, electron charge and electron wavelength, respectively. The electron wavelength $\lambda = h / mv = h / (2meV)^{1/2}$,

where V (in Volts) is the accelerating voltage. For V=200 kV, λ=0.002508 nm. N_z= number of unit cells in z-direction.

The interaction constant σ, represents the strength of interaction of electrons with matter. σ decreases with increasing voltage V . The phase shift $\Delta\Phi(x,y)$ depends on the voltage and reflects the projected potential of the crystal $\varphi(x,y)$. The wave function at the exit surface of the crystal can be written as

$$\psi_{ex} = \exp(-i\sigma N_z \varphi(x,y))$$

This wave can be expressed as a Taylor series:

$$\psi_{ex}(x,y) = 1 - i\sigma N_z \varphi(x,y) - \sigma^2 (N_z \varphi(x,y))^2/2 + \ldots$$

When the weak-phase object approximation is valid the amplitude of the wave function $\psi_{ex}(x,y)$ at the exit surface is proportional to the amplitude of the structure factor of the crystal, while the phase of $\psi_{ex}(x,y)$ is shifted by $(-\pi/2)$ with respect to the structure factor F(x,y). For the details see references [18-20].

2.3. High Resolution Imaging

In the image formation process [18], when the electron beam passes through the microscope we distinguish the following phenomena (see Fig. 1(a)):

- diffraction phenomena in the plane of the object,
- the image formation in the back focal plane of the objective lens,
- the interference, of diffracted beams, in the image plane of the objective lens.

The wave function $\psi_{ex}(r)$ of electrons at the exit face of the object can be considered as a planar source of spherical waves according to the Huygens principle. The amplitude of diffracted wave in the direction given by the reciprocal vector **g** is given by the Fourier transformation of the object function , i.e.

$$\psi(\mathbf{g}) = \Im_g \, \psi(\mathbf{r})$$

The intensity distribution in the diffraction pattern is given by $|\psi(\mathbf{g})|^2$ in the back focal plane of the objective lens.

$$|\psi(\mathbf{g})|^2 = |\Im_g \, \psi(\mathbf{r})|^2$$

If the object is periodic, the diffraction pattern, the square of the FT of the object function, will consist of sharp spots. In the second stage of the imaging process the back focal plane acts as a set of Huyghens sources of spherical waves which interfere, through a system of lenses, in the image plane. This stage in the imaging process is described by an inverse Fourier transform which reconstructs an enlarged object function $\psi(R)$. The intensity in the image plane is finally given by $|\psi(R)|^2$.

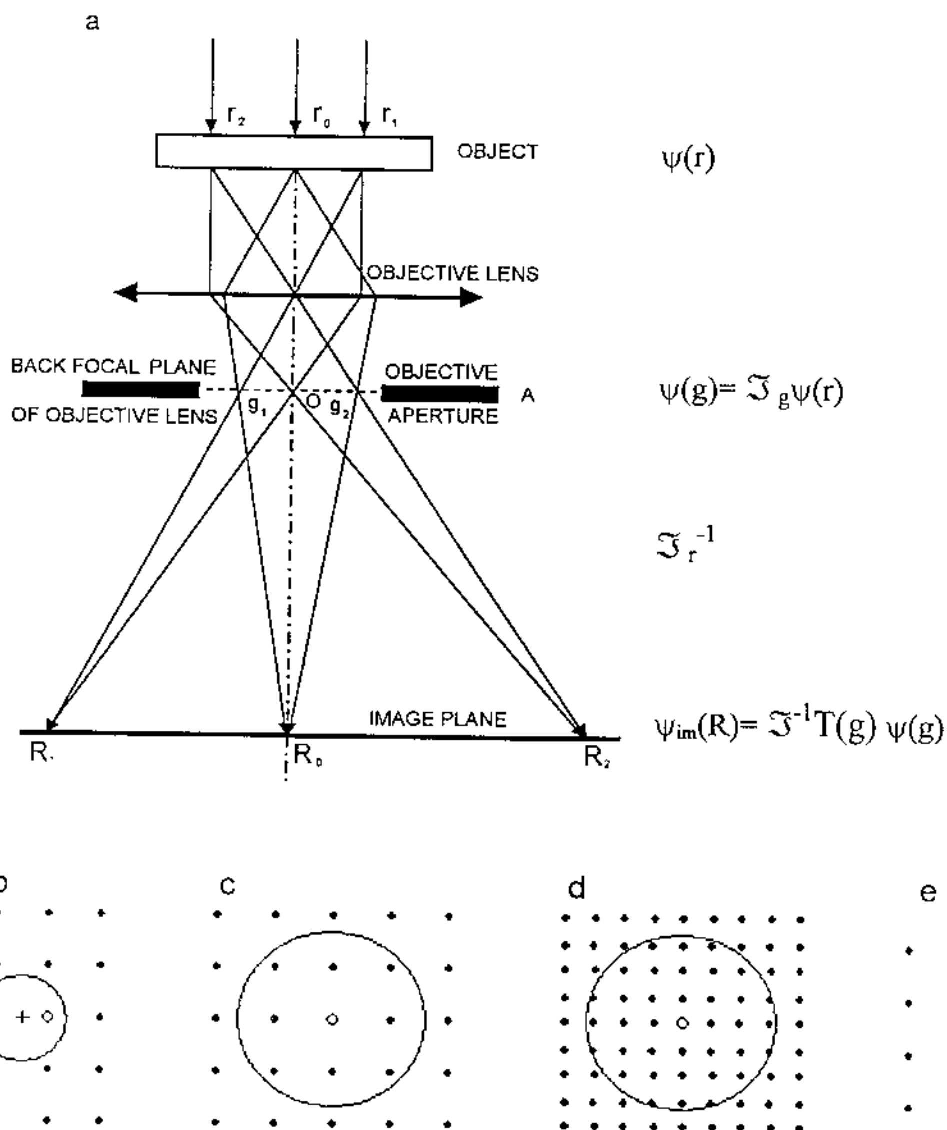

Figure 1: (a) Image formation in an electron microscope; (b, c, d, c,) schemes of diffraction patterns and aperture configurations; + - optical axis, **o** - undiffracted beam; **O** - objective aperture **A** as placed in (a).

During the second step in the image formation, which is described by the inverse Fourier transform, the electron beam undergoes a phase shift $\chi(\mathbf{g})$ with respect to the central beam. The phase shift is caused by spherical aberration and defocus and damped by incoherent damping function $D(\alpha,\Delta,\mathbf{g})$, so that the wave function $\psi_{im}(R)$ at the image plane is finally given by

$$\psi_{im}(R)= \Im^{-1}\, T(g)\, \psi\,(\mathbf{g})$$

where $T(\mathbf{g})$ is the contrast transfer function (CTF) of thin phase object.

$T(\mathbf{g})$ includes damping envelope $D(\alpha,\Delta,\mathbf{g})$ and phase shift $\chi(\mathbf{g})$:

$$\chi(\mathbf{g}) = \pi\varepsilon\,\lambda\mathbf{g}^2 + \pi\, C_s \lambda^3\, \mathbf{g}^4/2 \qquad T(\mathbf{g})= D(\alpha,\Delta,\mathbf{g})\, \exp\,[\,i\, \chi(\mathbf{g})\,]$$

α is the convergent angle of the incident electron beam and Δ is the half-width of the defocus spread ε due to chromatic aberration. For the details consult references [18-20].

The main experimental techniques in common use at present in the field of conventional high-resolution electron microscopy, in phase contrast, are given in Fig. 1 (b, c, d, e) [1]. The different imaging modes are determined by the size and geometrical position of the objective aperture in the back focal plane of the objective lens. A lattice fringe image is obtained, if only one (or a few) diffracted beams interfere with the unscattered beam (aperture type b). The period of fringes corresponds to the interplanar spacing of the excited beams. Using an aperture type c, a many-beam image will be observed. For thin crystal having large unit cell parameters under experimental conditions, obtained using aperture type d, the "structure image" could be obtained if the micrograph is directly interpreted in terms of the projected atomic arrangement of the crystal structure. A dark-field lattice image is formed if particular diffracted beams of interest interfere and all other beams are excluded; aperture type e.

2.4. Contrast Transfer Function (CTF)

The specimen-independent properties of the electron optical imaging system are characterised by the contrast transfer function (CTF). This function describes the phase shift of the electron wave due to the influence of the spherical aberration and

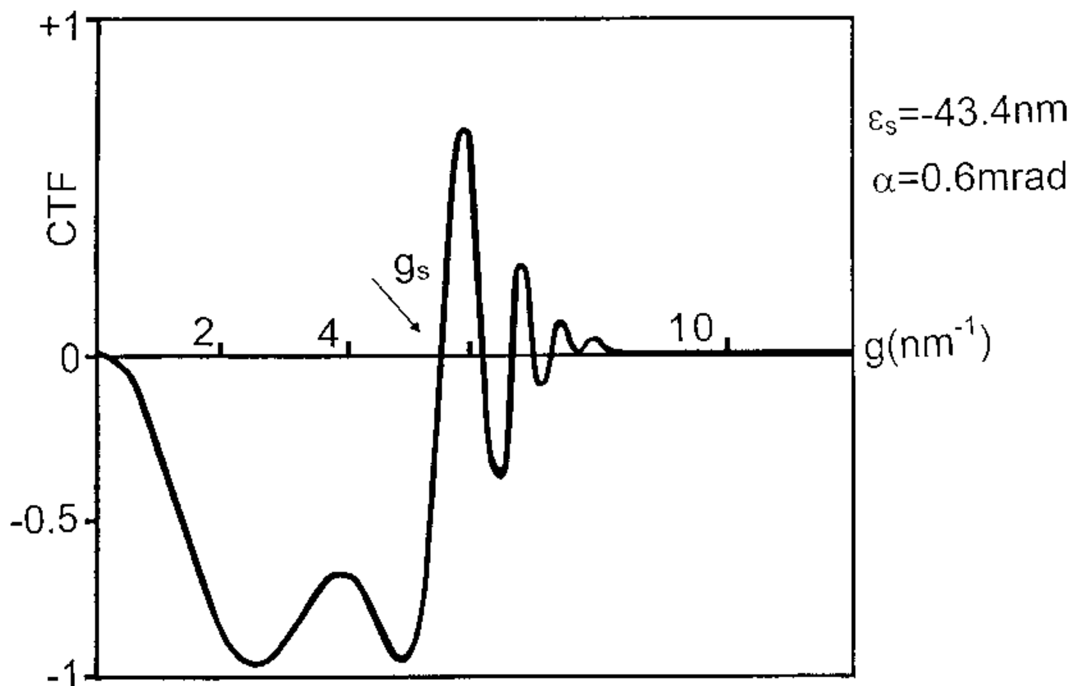

Figure 2: Contrast transfer function of JEOL JEM 2010 200 kV electron microscope: Scherzer underfocus $\varepsilon = -43.4$ nm, $\alpha = 0.6$ mrad, $g_s = 5\ nm^{-1}$.

defocusing of the objective lens. In the WPOA contrast transfer function T(g) is:

$$T(g) = \exp(i\chi(\mathbf{g})),\ \text{should be}\ \sin\chi(\mathbf{g})=1\ \text{and}\ \cos\chi(\mathbf{g})=0,\ \chi(\mathbf{g})=n\pi/2$$

for all **g**. Under this condition the intensity distribution will be an image of projected potential, and the double scattered electrons will be eliminated to contribute to the image [18-20].

The function $\sin\chi(\mathbf{g})$, which describes how the electron beams that leave the object are modified by the microscope and its variation with **g**, depends on the values of the parameters:

λ, C_s (constant of spherical aberration) and ε (the defocusing value).

It is possible to find a defocus ε that partly compensates for the spherical aberration, bringing $\sin\chi(\mathbf{g})$ to value -1, over an extended interval of **g**. This underfocus, i.e. negative value of ε, is the Scherzer focusing condition, the best possible approximation to the ideal case and the optimum setting for structure imaging with the correct contrast.

For this condition, the projected potential is proportional to the negative of the image intensity, i.e. black features in HRTEM positives (low intensity) correspond to atoms (high potential). Contrast transfer function of Jeol 2010 UHR 200 kV microscope, for Scherzer focusing condition of -43.4 nm is shown in Fig. 2.

CTF determines resolution and interval of d-values (interplanar spacing) to be transferred and imaged in the image plane of EM, by particular microscope adjustment determined by instrument and particular experimental conditions.

2.5. Resolution

Speaking about resolution:

a) point-to-point resolution or structure image resolution is a measure of the ability of the TEM to fatefully reproduce the structure of the sample as projected in the direction of the incident electron beam.

b) line (fringe) resolution, considers the smallest distinguishable separations between regularly spaced fringes. Such fringes are generated from the interference between two diffraction spots and have no sample correlation with the crystal structure other than reflecting a periodicity perpendicular to one crystallographic direction (See Fig. 1(b)).

The general expression for resolution d_s, for BF point-to-point resolution is

$$d_s = 0.67\,\lambda^{3/4} C_s^{1/4}, \qquad (1)$$

where λ is the electron wavelength and C_s is the coefficient of spherical aberration of the objective lens [16,18]. Improvements in resolution can be made by decreasing the wavelength and the spherical aberration. An increase in the accelerating potential decreases the wave length λ, but causes other problems such as power supply and instrumental instabilities.

Achieving a decrease in C_s requires the solution of extremely difficult pole-piece design and engineering problems, including the need for very small gaps into which to place the specimen. The result is that there is little or no space for tilting the specimen to obtain proper orientations.

Another view of resolution can be understood by considering the transfer function which is discussed and revealed in Fig. 2, so that the relation (1) for resolution is reciprocal of **g**-vector (spatial frequency) of the first zero of contrast transfer function, i.e. $d_s=1/g_s$, where g_s is the first zero of CTF and defines point-to-point resolution d_s of the EM (d_s= 0.197 nm in the case of JEOL 200 kV electron microscope).

3. An Application of HRTEM Image Processing in Analysis of Photographs of Mechanically Alloyed Materials

3.1. General Consideration

In pure zirconia ZrO_2, having monoclinic structure at room temperatures, the high temperature cubic phase is stable above 2370^0C and cannot be quenched to room temperature [21]. The stabilisation of the cubic phase at room temperature is possible by alloying zirconia with other oxides such as MnO, NiO, Cr_2O_3, Fe_2O_3, Y_2O_3, Ce_2O_3. However, a very high temperature (over 1000^0C) of calcination or sintering is required for preparation of solid solutions of zirconia with these oxides [22-24]. Y. L. Chen and D. Z. Yang showed [25] that mechanical alloying (MA) could also be used for alloying ceramic materials (ZrO_2-CeO_2 system), and recently we reported [26] that it is possible to synthesise ZrO_2-10mol.% of Y_2O_3 cubic solid solutions as the end product although in first stages of alloying the tetragonal phase appeared.

It is generally believed that alloying and amorphization are brought about by a solid state reaction during mechanical alloying, as a mixture of thin layers [27]. This is the same mechanism as that which occurs in thin films [28]. However, there is a lack of TEM and HRTEM results in the literature to confirm this model of alloying process [29,30].

In the present work the initial stage of the mechanical alloying process in ZrO_2-10mol%Y_2O_3 powders using HRTEM image processing is investigated. The results obtained by applying the CRISP program [13] to analyse HRTEM photographs of mechanically alloyed materials are presented [31-33]. The method described here could be applied in the investigation of any nanocrystalline materials.

3.2 Experimental Procedure TEM and HRTEM

Powders of zirconia and yttria were milled for 10 minutes in a Fritsch planetary micro-ball mill Pulverisette 7, as reported previously [26,34]. The resulting specimens were examined by X-ray diffraction (PHILIPS PW 1820 diffractometer), by TEM and HRTEM (JEOL JEM 2010 electron microscope, equipped with an ultra high resolution pole-piece, operating at an acceleration voltage of 200 kV, a C_s of 0.5 mm and a point resolution of 0.19 nm).

X-ray diffraction (XRD) in ZrO_2-10mol%Y_2O_3 powders, ball milled for 10 minutes, showed evidence of the formation of tetragonal zirconia solid solution (t-ZrO_2 SS) [26,33]. From previous TEM, HRTEM and electron diffraction (ED) measurements [33] an evidence on the microstructure in different regions of the sample was obtained. The agglomeration t-ZrO_2 and Y_2O_3 (from 7 to 60 nm) grains being attached to a large m-ZrO_2 grain are observed. The layered structure, induced by ball milling, revealed the shear deformation of lattice planes and planes ruptures. The small flakes of material having 10 nm size had, according to ED [26], a tetragonal nanocrystalline structure. These first grains of t-ZrO_2 solid solution nucleated at m-ZrO_2 layers.

3.3. Image Processing of HRTEM Photographs

A further insight was obtained into the alloying process by image processing of HRTEM photographs. One example from the early stages of the milling process will be given. During milling, fragmentation and adhesion of the grains is a steady process. However, the newly formed interfaces between monoclinic zirconia grains and Y_2O_3 grains can be brought into the intimate contact by subsequent ball collision forming an agglomeration, composed of grains G, C, M and region D. Fig. 3(a) shows a large monoclinic grain, M, nearly in the $[0\bar{1}\bar{1}]$ orientation. From this region two selected area diffraction photographs (SAD), shown in Figs. 3(b) and 3(c), were taken. In the SAD pattern the strongest reflections belong to the m-ZrO_2 grain, M, and the weak reflections belong to the Y_2O_3 layer, L, in $[01\bar{1}]$ orientation. The region marked L

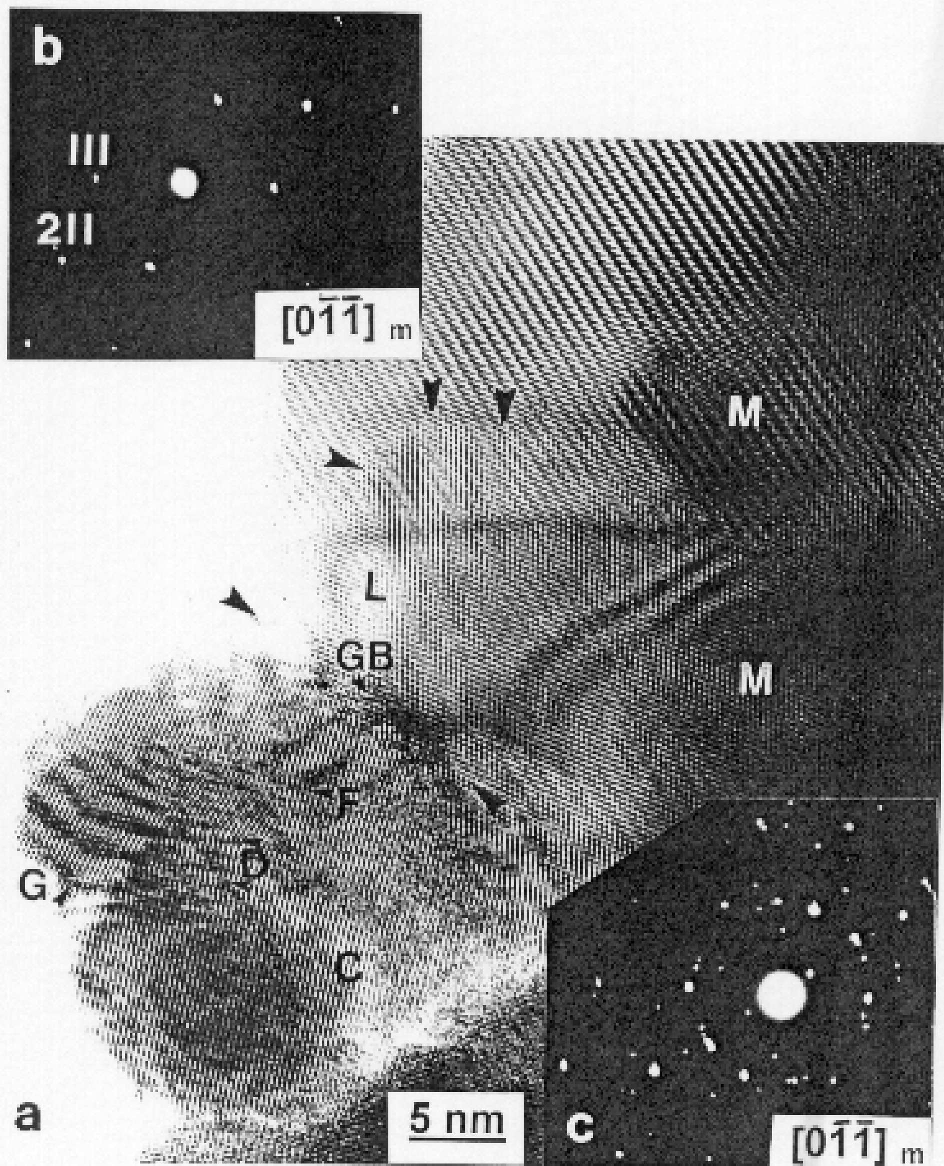

Figure 3. (a) HRTEM photograph of mixture of m-ZrO_2 and Y_2O_3 powders ball milled for 10 min; (b) ED pattern of (a) [0 $\bar{1}$ $\bar{1}$] m-ZrO_2; (c) ED pattern of (a) nearly [0 $\bar{1}$ $\bar{1}$] m-ZrO_2 ‖ [01 $\bar{1}$] Y_2O_3 zone. The meaning of lettering explained in the text.

is composed of m-ZrO_2 grain overlapped with the thin layer of Y_2O_3 in [01$\bar{1}$] orientation, which may serve as an evidence that alloying takes place in layers. Some other nanocrystalline Y_2O_3 grains distributed in the aggregate give additional spots, which form very sparse, spotty rings in the SAD pattern shown in Fig. 3(c).

The image processing analysis of this HRTEM image showed that further atomic mixing occurred at the grain boundary (GB) region as well as in the layers. Previously, it was also revealed [29,30], using HRTEM and EDS (energy dispersive X-ray analysis), that layered structures are formed in ball milled samples.

To elucidate the process of the solid-state reaction during ball-milling one has wanted to find out how Y_2O_3 penetrates into the m-ZrO_2 lattice and how this results in the formation of a tetragonal ZrO_2 solid solution (t-ZrO_2 SS). The diffraction pattern was calculated, i.e. the Fourier transform (FT), of the sample image. Each distinctive set of planes in the image will give a Fourier component in the calculated diffraction pattern, a bright spot (a "reflection") with a given amplitude and phase. Filtering of the spots in the diffraction pattern allows individual features in the original image to be reconstructed.

This method of filtering is a very general approach, and has been used in optical microscopy [34] and in electron microscopy [35]. In this approach, the crystal lattice of the specimen is considered as being built up of a number of gratings, each with its own spacing *d*. Image formation in the electron microscope proceeds by the formation of a series of maxima in the back focal plane of the objective lens, each maximum having its own amplitude and phase. Recording this pattern would give the electron diffraction pattern, although phase information would be lost. However, if the electron beams then pass through the objective lens, they form the image.

The CRISP approach [13] to image processing is the inverse procedure. The calculated Fourier transform of the image corresponds to the ED pattern, with the important property that the phase information is preserved. Each of the gratings in the crystal lattice has given rise to a set of fringes in the image, and the calculated Fourier transform will contain one bright spot corresponding to each set of fringes. By selectively preserving information in the reflections, one can obtain information about the fringes in the image, and consequently also information about the structure of the crystal lattice. In particular, one can obtain information about a particular family of crystal planes.

The Fourier transforms of several regions in Fig. 3(a) were calculated. The regions selected for study are marked in Fig. 3(a) as:

1. The grain boundary, GB,
2. A region, L, of overlapping layers of zirconia and yttria,
3. A region, F, containing stacking faults.

The Fourier transforms of regions of size 256 x 256 pixels (corresponding to around 6x 6 nm^2 in the specimen) were calculated. In each FT, masks with holes of radius 5 pixels were used to select components of the FT. The effect of hole size was investigated within a range from 1 to 5 pixels, the largest size being chosen in order to ensure that very large reflections from the ZrO_2 were completely encircled by the mask hole.

1. Grain boundary region: The Fourier transform of the grain boundary region is shown in Fig. 4(d) and contains the reflections from the ED pattern shown in Fig. 3(b). The reflections in the FT are marked by numbers 1 to 7, and are assigned to m-ZrO_2 and Y_2O_3, as shown in Table 2. The reflections marked 2, 3, 6 and 7 were complex spot containing identifiable components whose values are assigned in the Table 2.

The results obtained after filtering using particular reflections are displayed in Figs. 4(a) to 4(l). Fig. 4(a) shows the ($\bar{1}$11) lattice image of m-ZrO_2, which is obtained using reflection 1. Similarly, Fig. 4(b) shows the (111) lattice image of m-ZrO_2 and (222)Y_2O_3, which are obtained using complex reflection 2. Fig. 4(c) is superposition of lattice images in reflections 1 and 2 as given in Figs. 4(a) and 4(b). Fig. 4(d) is FT of GB region. Fig. 4(e) shows the lattice image from reflections 3, that contain ($\bar{1}$11) m-ZrO_2 and (222)Y_2O_3. Fig. 4(f) shows superposition of images in reflections 1, 2 and 3.

Two sets of planes from Y_2O_3 are shown in Figs. 4(g) and 4(h), corresponding to reflections 4 and 6. These two reflections are combined in the reconstruction shown in Fig. 4(i) in order to reveal the appearance of yttria in the grain boundary region. Figs. 4(k) and 4(l) are reconstructed images with all reflections from FT Fig. 4(d) and with all marked reflections, respectively. Unfiltered original image, Fig. 4(j) should be compared to Figs. 4(k) and 4(l). We can follow successive formation of the final HRTEM image by making the comparison of Figs. 4(f) and 4(i) to Fig. 4(l) and to the original

image given in Fig. 4(j). Here using a HRTEM image processing of original image we revealed and proved how "alloying" took place in the GB.

TABLE 1

d-values Assignment Obtained From FT (Figure 4(d)) of the Grain Boundary Region

spot in FT	*d* measured (nm)	calculated indices hkl	phase identified	*d*(nm) from literature	corresponding lattice image
1	0.3115	$\bar{1}11$	m-ZrO_2	0.316	Figure 4(a)
2	0.282-0.299	111	m-ZrO_2	0.284	Figure 4(b)
		222	Y_2O_3	0.306	
3	0.298	$\bar{1}11$	m-ZrO_2	0.316	Figure 4(e)
		222	Y_2O_3	0.306	
4	0.2237	332	Y_2O_3	0.226	Figure 4(g)
5	0.361	011	m-ZrO_2	0.364	
6	0.277	400	Y_2O_3	0.265	Figure 4(h)
		111	m-ZrO_2	0.284	
7	0.189	440	Y_2O_3	0.187	
		220	m-ZrO_2	0.185	

2. Overlapping layers L of zirconia and yttria: The electron diffraction pattern shown in Figs. 3(b) and 3(c) is close to the $[0\bar{1}\bar{1}]$ zone of m-ZrO_2 lattice. The faint reflections are due to Y_2O_3. It is not obvious whether the large grain M has a thin layer of Y_2O_3 overlapping it. Furthermore, one wanted to explain why the different regions of the grain M have different appearances, by determining the constituents of the HRTEM pattern. Fourier transform of different parts with masks having sizes 256 x 256 pixels and 512 x 512 pixels was performed. All Fourier transforms from this region had the same appearance (Fig. 5(j)), showing that the two zones, one from yttria and one from zirconia, are parallel, and that the layers are parallel. The reflections in the FT are marked by numbers from 1 to 7, and are assigned to m-ZrO_2 and Y_2O_3 , as shown in Table 2.

The results obtained after filtering using particular reflections from FT of Fig. 5(j) are displayed in Figs. 5(a) to 5(l).

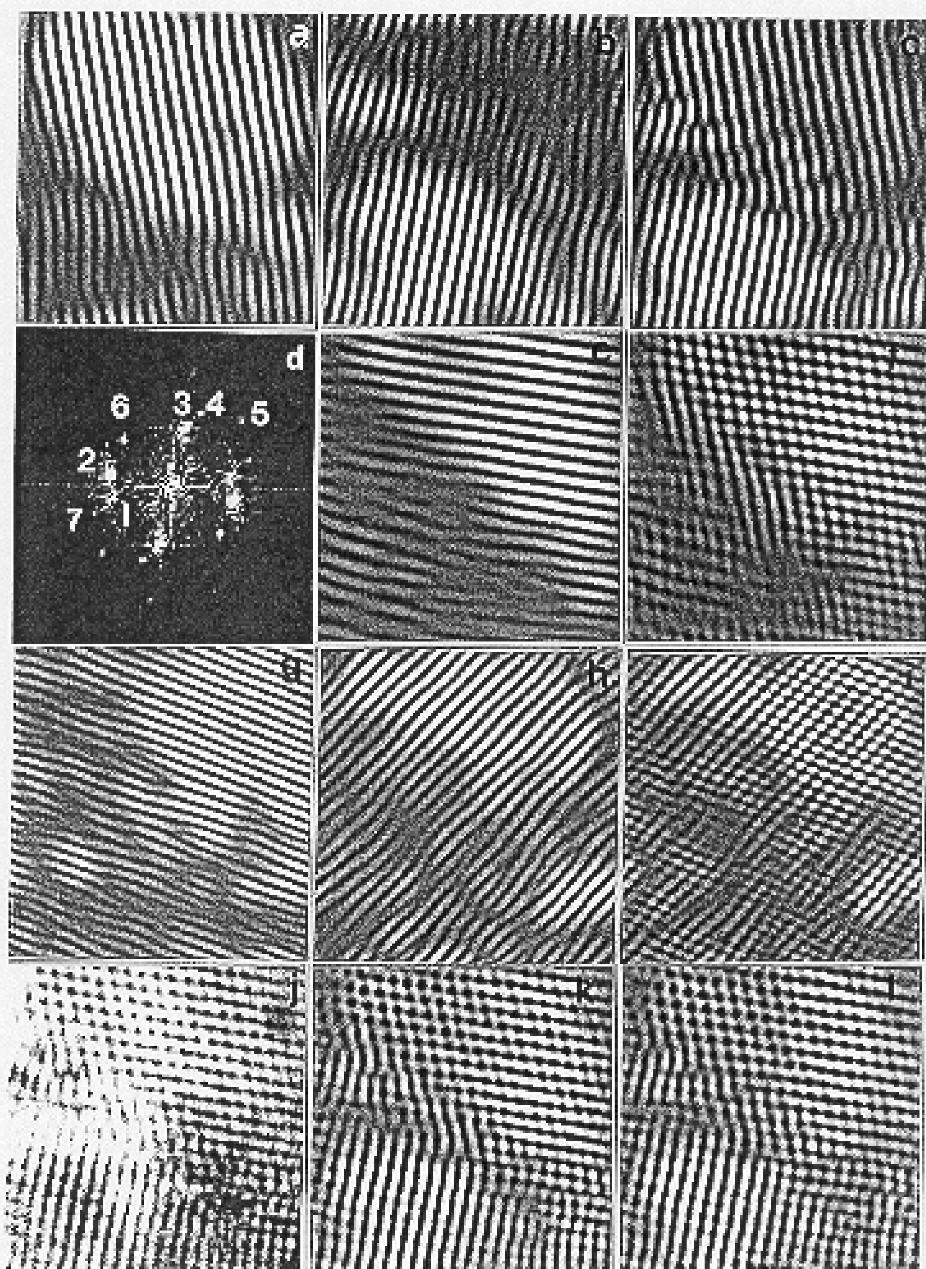

Figure 4. The filtered lattice images from the grain boundary GB region obtained with particular diffraction spots from FT of Fig. 4(d): (a) 1 - ($\bar{1}$11)m-ZrO_2 , d=0.316 nm; (b) 2 - (111)m-ZrO_2 and (222)Y_2O_3 ; (c) superposition of lattice images given in (a) and (b); (d) FT of GB region; (e) 3 - ($\bar{1}$11) and (222)Y_2O_3 , d=0.3 nm; (f) superposition of images in reflections 1, 2 and 3 from (a) , (b) and (e); (g) 4 - (332)Y_2O_3 , d=0.226 nm; (h) 6 - (400)Y_2O_3 , d=0.265 nm; (i) superposition of lattice images of Y_2O_3 reflections 4 and 6 from (g) and (h); (j) unfiltered original image; (k) all reflections from FT (d); (l) all marked reflections from FT.

TABLE 2

d-values Assignment Obtained From FT (Figure 5(j)) of the Region of Layer L

spot in FT	*d* measured (nm)	calculated indices hkl	phase identified	*d*(nm) from literature	corresponding lattice image
1	0.19	440	Y_2O_3	0.187	Figure 5(a)
		400	Y_2O_3	0.265	
2	0.265-0.247	200	m-ZrO_2	0.262	Figure 5(b)
3	0.256-0.246	400	Y_2O_3	0.265	Figure 5(c)
4	0.426	$\bar{2}11$	Y_2O_3	0.434	Figure 5(d)
5	0.435	211	Y_2O_3	0.434	Figure 5(e)
6	0.315	$\bar{1}11$	m-ZrO_2	0.316	Figure 5(h)
7_1	0.302-0.299	$\bar{1}11$	m-ZrO_2	0.316	
7_2	0.299	222	Y_2O_3	0.306	Figure 5(g)
7_3	0.323	$\bar{1}11$	m-ZrO_2	0.316	

Fig. 5(a) shows the (440) lattice image of Y_2O_3, which is obtained using reflection 1. Similarly, Fig. 5(b) shows the (200) lattice image of m-ZrO_2, which is obtained using reflection 2, although the identification of this reflection is uncertain, and an alternative explanation could be (400) from Y_2O_3. Fig. 5(c) shows the (400) lattice image of Y_2O_3 from reflection 3. Two symmetry related sets of planes from Y_2O_3 are shown in Figs. 5(d) and 5(e), corresponding to reflections 4 and 5. These two reflections are combined in the reconstruction shown in Fig. 5(f). Fig. 5(h) shows the reconstruction from reflection 6, the ($\bar{1}11$) from m-ZrO_2, while Fig. 5(g) shows the reconstruction obtained from three reflections 7. The reconstruction using both reflection 6 and reflections 7 is shown in Fig. 5(i).

Fig. 5(k) shows the reconstruction obtained when using contributions both from yttria and from m-ZrO_2, reflections 4, 5, 6 and 7_1, 7_2, 7_3. Finally, Fig. 5(l) shows the reconstruction obtained with all the reflections identified in the FT (Fig. 5(j)). One can see that this image reveals stripped details from the original HRTEM photograph of Fig. 3 in the region marked L.

Fig. 5(l) shows a periodicity of 0.74 nm, arising from the superposition of yttria and zirconia reflections. The Fourier transform and the ED pattern of this region

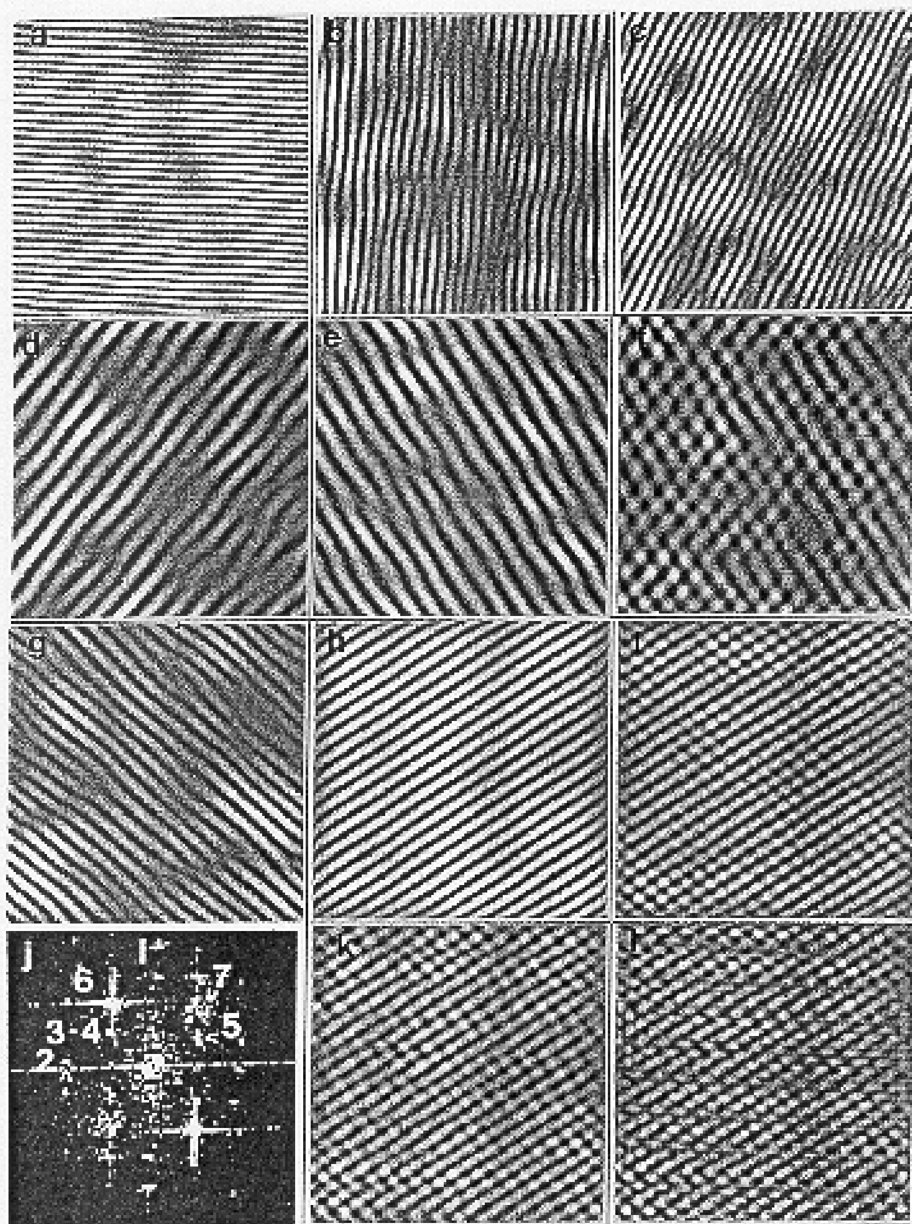

Figure 5. Filtered lattice images of the overlapping layers L obtained with particular diffraction spots from FT of Fig. 5(j): (a) 1 - (440)Y_2O_3, d=0.187 nm; (b) 2 - (200)m-ZrO_2, d=0.262 nm; (c) 3 - (400)Y_2O_3, d= 0.265 nm; (d) 4 - ($\bar{2}$11)Y_2O_3, d=0.434 nm; (e) 5 - (211)Y_2O_3, d=0.434 nm; (f) superposition of images of yttria from (d) and (e); (g) 7_1, 7_2, 7_3 - ($\bar{1}$11)m-ZrO_2, d=0.316 nm, (222)Y_2O_3, d=0.306 nm, ($\bar{1}$11)m-ZrO_2, d=0,316 nm; (h) 6 - (1$\bar{1}$1)m-ZrO_2, d=0.316 nm; (i) the superposition of lattice images of m-ZrO_2 6 and 7 from (g) and (h): (j) FT of the region L; (k) reconstructed image with superposition of (f) and (i) images; (l) reconstructed original image with all reflections from FT (j).

have shown the strong streaked reflection from the $[0\bar{1}\bar{1}]$ zone of m-ZrO_2, while the faint reflections come from the $[01\bar{1}]$ zone of Y_2O_3 (see Fig. 3(c)). This zone is parallel to the $(0\bar{1}\bar{1})$ of m-ZrO_2 (see Fig. 3(c)), which means that the layers of zirconia and yttria are also parallel.

TABLE 3

d-values Assignment Obtained From FT (Figure 6(g)) of the Stacking Fault Region

spot in FT	*d* measured (nm)	calculated indices hkl	phase identified	*d*(nm) from literature	corresponding lattice image
1_1	0.316	$\bar{1}11$	m-ZrO_2	0.316	Figure 6(a)
1_2	0.265	200	m-ZrO_2	0.262	
		400	Y_2O_3	0.265	
2	0.369-0.3906	110	m-ZrO_2	0.369	Figure 6(d)
3	0.175-0.182	$\bar{1}22$	m-ZrO_2	0.178	Figure 6(e)
		022	m-ZrO_2	0.181	
		440	Y_2O_3	0.187	
4	0.2079	431	Y_2O_3	0.208	Figure 6 (c)

3. Stacking fault region: The results of filtering analysis of stacking fault region F are displayed in Figs. 6(a) to 6(i), while the *d*-values assignment obtained from FT of Fig. 6(g) are given in Table 3. Elongated spot ("streak") in FT of Fig. 6(g) cut in the Fourier space region, giving in real space the *d*-values from 0.316 to 0.266 and it could be regarded as a complex broadened spot containing at least two components 1_1 and 1_2 (as noted in Table 3) of the planes having meeting point at the stacking fault. As the lattice image in the reflection 3 was assigned as a mixture of m-ZrO_2 and Y_2O_3 reflections, one can see in the Fig. 6(e) that corresponding planes (as identified in Table 3) are introduced as the dislocations in Fig. 6(e). In Fig. 6(f) the superposition of images given in Figs. 6(d) and 6(e) are shown revealing interwoven m-ZrO_2 and Y_2O_3 planes originated from reflections 2 and 3.

As there is a change in the contrast at stacking fault, it is probable that the nucleation of new t-ZrO_2 SS phase took place at stacking fault F, so the Y_2O_3

segregates on defects in m-ZrO_2 lattice that is revealed in the filtering analysis as penetration of Y_2O_3 and ZrO_2 planes as assigned in Table 3 and revealed in Fig.6 (f). The presence of Y_2O_3 (400) planes in Fig. 6(b) and (440) planes in Fig. 6(c) at stacking faults means that segregation of yttria on stacking faults in m-ZrO_2 is a possible process.

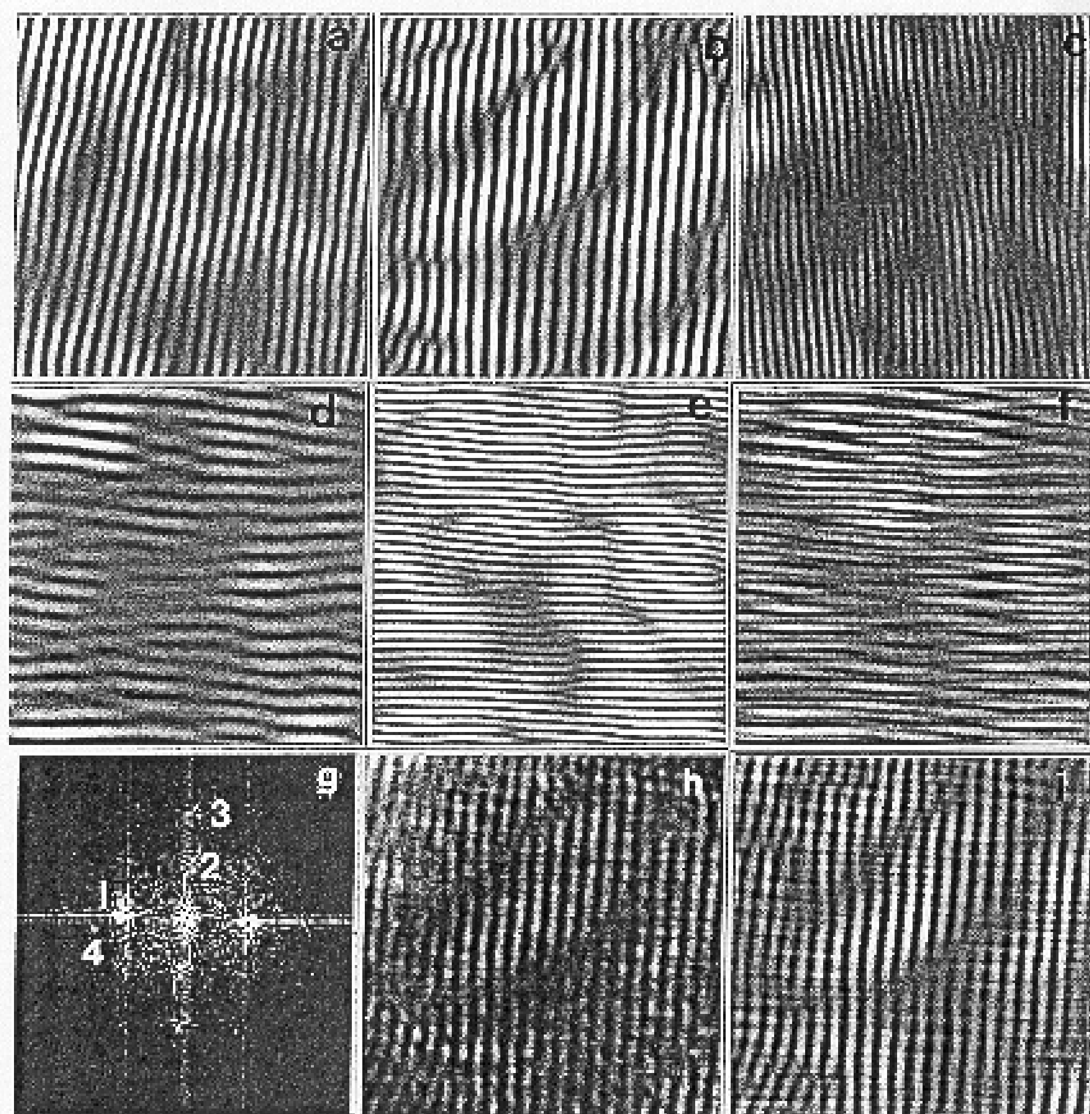

Figure 6. The filtered lattice images from the stacking fault region obtained with particular diffraction spots from FT of Fig. 6(g): (a) 1_1 - ($\bar{1}$11)m-ZrO_2 , d=0.316 nm; (b) 1_1+1_2 - ($\bar{1}$11)m-ZrO_2 , (200)m-ZrO_2 and (400)Y_2O_3; (c) 4 - (431)Y_2O_3, d=0.208 nm ; (d) 2 - (110)m-ZrO_2 , d=0.369 nm; (e) 3 - m-ZrO_2 + Y_2O_3 , d=0.18 nm; (f) superposition of images (d) and (e); (g) FT of stacking fault region; (h) stacking fault - original image; (i) reconstruction of original image with all reflections from FT (g).

3.4. Refinement of Filtering Analysis

Spot 7, in the Fourier transform (FT) of the overlapping layers L, shown in Fig. 5(j) is a multiple spot consisting of three components, and the reconstruction shown in Fig. 5(g) is obtained when all three components are used.

Fig. 7 shows filtered images obtained using mask holes which allow different components of reflection 7 to contribute. Fig. 7(a) shows the reconstruction obtained with a hole of one pixel radius, which isolates the $(\bar{1}11)$ planes of the m-ZrO_2 lattice.

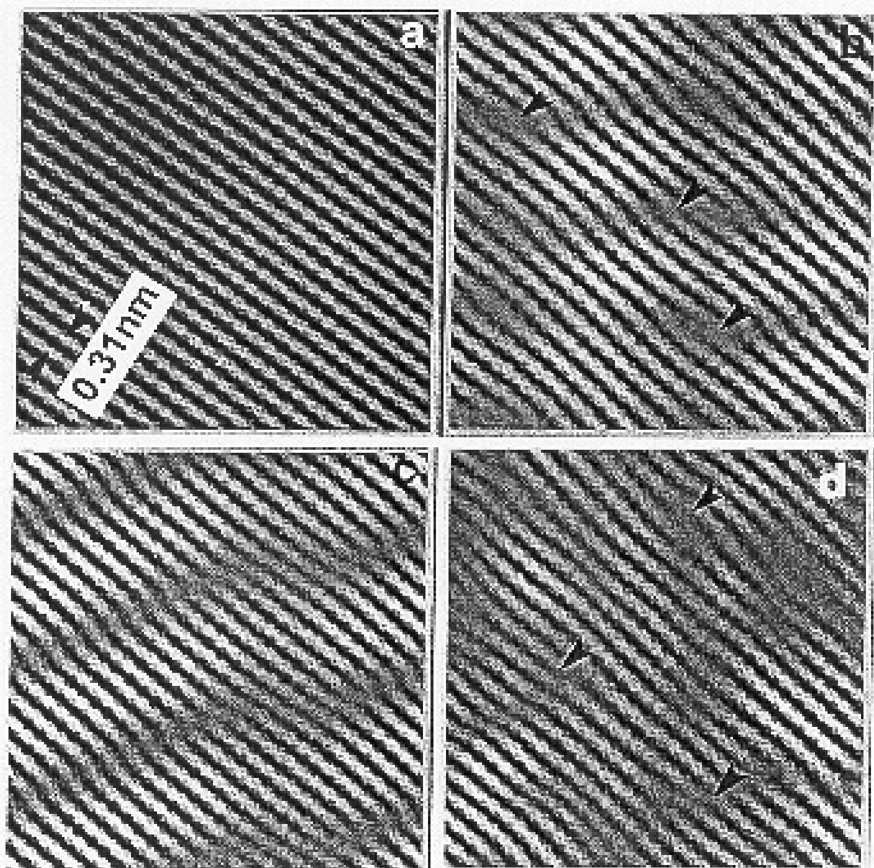

Figure 7. Refinement in overlapping layers L. Filtered lattice images with spots 7 $(7_1,7_2,7_3)$: $(\bar{1}11)$ m-ZrO_2, (222) Y_2O_3, $(\bar{1}11)$ m-ZrO_2 from FT of Fig. 5(j) with different filtering mask radius: (a) $(\bar{1}11)$ m-ZrO_2 (d=0.316 nm), one pixel; (b) all spots 7, three pixel; (c) two spots 7_1 and 7_2, isolated with one pixel mask; (d) five pixels encircling all three spots 7.

The lattice planes of m-ZrO_2 appear perfect without any distortion. A hole of size three pixels was used to obtain the reconstruction shown in Fig. 7(b), allowing all three components of reflection 7 to contribute. Two components of reflection 7, 7_1 and 7_2, were allowed to contribute to the reconstruction shown in Fig. 7(c), using two separate holes each of radius one pixel, while Fig. 7(d) shows the reconstruction obtained with a hole of radius 5 pixels.

Image processing, in particular the use of Fourier filtering, has given a new insight into the fine details of HRTEM images, allowing us to draw conclusions about the physical processes occurring in the initial stages of mechanical alloying induced by ball milling. Figs. 7(a) to 7(d) give information about the rupturing of the $(\bar{1}11)$ m-ZrO_2 planes, i.e. about insertion of other $(\bar{1}11)$ planes of ZrO_2 and penetration of (222) planes of Y_2O_3 into $(\bar{1}11)$ m-ZrO_2 planes. The images shown in Figs. 7(a) to 7(d) allow the following physical interpretation. The rupture of planes in ball milled samples occurs initially at the level of 2.5 to 3 nm, shown by arrows in Figs. 7(b) to 7(d). We can identify intercalated planes having origin in other m-ZrO_2 and Y_2O_3 grains. These planes, indexed according to corresponding FT, break into the perfect order of the $(\bar{1}11)$ monoclinic ZrO_2 lattice planes observed in Fig. 7(a).

3.5. Conclusions

In the first part of the paper the basic terms needed in order to understand the high resolution electron microscopy method are described.

Because the knowledge of microstructure (defects, grain sizes,...) is indispensable for understanding the macroscopic behaviour of solids, in the second part of the paper the application of HRTEM image processing to the investigation of nanocrystalline materials is presented. Micrographs of the mechanically alloyed ZrO_2 -Y_2O_3 powders, in the initial stage of the transformation, were chosen for the HRTEM image processing analysis.

In this example one was able to show how, by using the HRTEM image processing analysis, it was possible to deduce the following:

1. Alloying of monoclinic zirconia and yttria and the formation of a new tetragonal ZrO_2 solid solution occur simultaneously.

2. Nucleation of the new tetragonal ZrO_2 solid solution occurs in the form of small layers having 10 nm in diameter.

3. The decrease of grain sizes is accompanied by stresses in the ball milling procedure when the defects or stacking faults are formed. This conclusion is supported by the results of the Fourier filtering analysis where inserted planes and broken planes are observed (Figs. 7(c) and 7(d)). These intercalated planes are assigned to particular planes according to the corresponding FT of the region.

4. In the grain boundary region one reveals the beginning of the alloying process as the inter-penetration of Y_2O_3 and m-ZrO_2 planes (Fig. 4(h) and Table 1). Some $(\bar{1}11)$ m-ZrO_2 planes traverse the grain boundary (Fig. 4(a)), while others are broken. The broken planes form stacking faults, which accommodate the newly formed interface between grains.

5. The refinement of Fourier filtering offers a new insight into the fine details of HRTEM images, allowing one to draw conclusions about the physical processes occurring in the initial stages of mechanical alloying induced by ball milling. The rupture of planes in ball-milled samples occurs initially at the level of 2 to 3 nm (Figs. 7(b) and 7(d)).

6. From the refinement analysis of Fig. 7 it follows that the inserted planes i. e. dislocations of Figs. 4(g) and 4(h), having origin in ZrO_2 or Y_2O_3 planes, identified in corresponding FT, show that the formation of dislocations in GB region represent one of the tentative mechanisms of alloying, reported recently [37]. The other mechanism of alloying proceeds via the segregation of Y_2O_3 on the stacking faults in m-ZrO_2.

As the final remark, one concludes that the HRTEM with image processing is a sensitive and precise method for the analysis of grain boundaries and defects, including stacking faults and overlapping layers, as well as for obtaining results which are inaccessible with other methods.

However, the other method of image processing [38] proposed recently is shown to be a suitable technique to provide a quantitative measurement of the sizes of ordered regions that are superposed in projections.

References

[1] W. Neumann, R. Hillebrand, P. Werner, *Electron Microscopy in Solid State Physics*; Elsevier, Amsterdam, 1987, pp 97-142.
[2] B. K. Vainstein, Z. G. Pinsker, *Journ. Phy. Chem (SSSR)* **1949**, *23*, 1058.
[3] D. J. DeRosier, A. Klug, *Nature (London)* **1968**, *217*, 130 -134.
[4] R. Henderson, N. Unwin, *Nature* **1975**, *257*, 28-32.
[5] S. Hovmöller, A. Sjögren, G. Farrants, M. Sundberg, B. O. Marinder, *Nature (London)* **1984**, *311*, 238-241.
[6] K. H. Downing, H. R. Meisheng, H. R. Wenk, M. A. O'Keefe, *Nature* **1990**, *348*, 525-528.
[7] H. R. Wenk, K. H. Downing, H.R. Meisheng, M. A. O'Keefe, *Acta Cryst.* **1992**, *A48*, 700-716.
[8] T. E. Weinreich, R. Ramlau, A. Simon, S. Hovmöller, X. D. Zou, *Nature* **1996**, *382*, 144-146.
[9] J. C. H. Spence, *Acta Cryst.* **1993**, *A49*, 231- 260.
[10] M. Tanaka, *Acta Cryst.* **1994**, *A50*, 261- 286.
[11] F. Phillipp, R.Höschen, M. Osaki, G. Möbus, M. Rühle, *Ultramicroscopy* **1994**, 56, 1-10.
[12] F. Phillipp, R. Höschen, M.Osaki, M. Rühle, *Electron Microscopy 1994, Vol 1, Proceed. 13th International Congress on Electron Microscopy*; Les Editions de Physics Les Ulis, Paris, France, 1994, pp 231-232.
[13] S. Hovmöller, *Ultramicroscopy* **1992**, *41*, 121-136.
[14] A. J. W. Edington, *Monographs in Practical Electron Microscopy in Materials Science*; Univ. Cambridge, England, 1975, Vol. 2 and 3, pp 1-75.
[15] L. Reimer, *Transmission Electron Microscopy, Physics of Image Formation and Microanalysis*; Springer -Verlag, Berlin-Heidelberg, 1989.
[16] P. R. Buseck, *Minerals and Reactions at the Atomic Scale, Transmission Electron Microscopy*; Mineralogical Society of America, Washington D. C., 1992, pp 1-111.
[17] J. Thibault, *High-Resolution Electron Microscopy, Lectures on ESMAT*; Oleron, France, 1992.
[18] J. M. Cowley, *Electron Diffraction Techniques, High Resolution Imaging*; International Union of Crystallography, Oxford University Press, Oxford, 1993, 131-169.
[19] L. Kihlborg, *Phase Contrast and High-Resolution electron microscopy*; Dep. Inorg. Chemistry, Stockholm University, 1995.
[20] X. D. Zou, *Ph.D. Thesis*; Stockholm University, 1995.
[21] E. C. Subbaro, H. S. Maiti, K. K. Srivastava, *Phys. Stat. Sol. (a)* **1974**, *21*, 9-29.
[22] A. Keshavaraja, A. V. Ramaswamy, *J. Mater. Res.* **1994**, *9*, 837-840.
[23] M. C. Caracoche, P. C. Rivas, A. P. Pasquevich, A. R. Lopez Garcia, *J. Mater. Res.* **1993**, *8*, 605-610.
[24] H. J. Fecht, *Nature* **1992**, *356*, 133-135.
[25] Y. L. Chen, D. Z. Yang, *Scripta Metall.* **1993**, *29*, 1349-1355.
[26] A. M. Tonejc, A. Tonejc, *Mater. Sci. Forum* **1996**, *225-227*, 497-502.
[27] P. J. Desré, A. R. Yavary, *Phys. Rev. Lett.* **1990**, *64*, 1533-1536.
[28] A. R. Yavary, P. J. Desré, *Mater. Sci. Eng* **1991**, *A134*, 1315-1322.
[29] A. M. Tonejc, D. Bagović, M. Tudja, *Mater. Lett.* **1994**, *20*, 51-61.
[30] J. Eckert, L. Schulz, K. Urban, *J. Non-Cryst. Solids* **1991**, *130*, 273-283.
[31] A. M. Tonejc, A. Tonejc, G. W. Farrants, S. Hovmöller, *Electron Microscopy 96, Proceedings 11th EUREM in Dublin, Vol. 2, Materials Sciences*; Charenton-le-Pont, France, 1998, pp 11-12.
[32] A. M. Tonejc, A. Tonejc, G. W. Farrants, S. Hovmöller, *Mater. Sci. Forum*, **1998**, *269-272*, 357-362.
[33] A. M. Tonejc, A. Tonejc, G. W. Farrants, S. Hovmöller, *Croat. Chem. Acta* **1999**, *72*, in press.
[34] A. Tonejc, A. M. Tonejc, D. Duževič, *Scripta Metall. et Mater.* **1991**, *25*, 1111- 1114.

[35] K. Kranjc, *American J. Physics* **1962**, *30*, 342-347.
[36] R. D. Heidenreich, *Fundamentals of Transmission Electron Microscopy*; Interscience Publishers, New York, 1964, pp. 138.
[37] R. B. Schwartz, *Mater. Sci. Forum* **1998**, *269-272*, 665-674.
[38] X. Pan, W. D. Kaplan, M. Rühle, R. E. Newnham, *J. Am. Ceram. Soc.* **1998**, *81*, 597-609.

Povzetek

V članku je podan kratek pregled uporabnosti visokoločljivostne transmisijske elektronske mikroskopije (HRTEM) s poudarkom na principu nastanka HRTEM slike v elektronskem mikroskopu, različnih načinih formiranja slike, vlogi elektronsko-optičnih parametrov pri nastanku HRTEM slike ter metodah za izboljšanje nivoja informacije. Kot primer kvantitativnega ovrednotenja HRTEM slik je podan študij fazne transformacije pri mehanskem preoblikovanju prahov ZrO_2 z 10 mol% Y_2O_3.
V pričujočem delu ja prikazana analiza HRTEM slik mehansko preoblikovanih nanokristaliničnih materialov z uporabo programskega paketa CRISP s poudarkom na: (a) mejah med zrni, (b) zlogovnih napakah in (c) prekrivajočih se plasteh Y_2O_3 in ZrO_2.
Analiza fourierjevo filtriranih eksperimentalnih mrežnih slik kaže na možen način preraščanja obeh faz na mejah med zrni, na zlogovnih napakah in prekrivajočih se domenah Y_2O_3 in ZrO_2. Z uporabo fourierjevih mask različnih velikosti smo uspeli izolirati različne sete ravnin Y_2O_3 in ZrO_2, ki so vraščene v monoklinskem ZrO_2. Vraščanje teh ravnin se odraža v tvorbi dislokacij, ki se pojavijo v povsem določeni medsebojni oddaljenosti v sicer perfektni mreži monoklinskega ZrO_2. Na osnovi teh rezultatov je podan možen mehanizem transformacije pri mehanskem preoblikovanju ZrO_2 in Y_2O_3.